Closed-Form Expressions for the Radiation Properties of Nanoloops in the Terahertz, Infrared and Optical Regimes

Bing Qian Lu, *Student Member, IEEE*, Jogender Nagar, *Student Member, IEEE*, Taiwei Yue, *Student Member, IEEE*, Mario F. Pantoja, *Senior Member, IEEE*, and Douglas H. Werner, *Fellow, IEEE*

***Abstract*— Since the pioneering work of Heinrich Hertz, perfect-electric conductor (PEC) loop antennas for RF applications have been studied extensively. Meanwhile, nanoloops are promising in the optical regime for their applications in a wide range of emerging technologies. Unfortunately, analytical expressions for the radiation properties of conducting loops have not been extended to the optical regime. This paper presents closed-form expressions for the electric fields, total radiated power, directivity, and gain for thin-wire nanoloops operating in the terahertz, infrared and optical regimes. This is accomplished by extending the formulation for PEC loops to include the effects of dispersion and loss. The expressions derived for a gold nanoloop are implemented and the results agree well with full-wave computational simulations, but with a speed increase of more than 300×. This allows the scientist or engineer to quickly prototype designs and gain a deeper understanding of the underlying physics. Moreover, through rapid numerical experimentation, these closed-form expressions made possible the discovery that broadband superdirectivity occurs naturally for nanoloops of a specific size and material composition. This is an unexpected and potentially transformative result that does not occur for PEC loops. Additionally, the Appendices give useful guidelines on how to efficiently compute the required integrals.**

***Index Terms*— Antenna theory, loop antennas, nanotechnology, submillimeter wave technology.**

I. Introduction

WIRELESS communications are expected to play a key role in the future development of practical nanotechnology-enabled devices, with applications ranging from energy harvesting to implantable medical devices [1]. The design of nanoantennas is particularly challenging for integration with such devices, which may be targeted for operation anywhere from the optical to terahertz regimes [2]. Metals no longer behave like perfect electric conductors (PECs) at these frequencies, instead exhibiting substantial dispersion and loss [3]. This has a dramatic impact on the radiation properties of nanoantennas, including directivity, efficiency, and total radiated power [4]. Antennas in the RF regime have been rigorously studied, and systematic design procedures exist [5]. The most popular and fundamental designs are the dipole and the loop, due to their simplicity, versatility, and utility in a wide variety of applications [6]. It has been found through simulation and measurement that these designs cannot simply be scaled to the optical regime—for example, optical dipoles resonate at lengths much shorter than one-half the wavelength [7]. In comparison to the large body of literature devoted to linear dipole-type nanowire antennas [7]–[8], much less work has been done to understand the radiation properties of nanoloop antennas. These structures are extremely promising for their potential applications in sensing [9], spectroscopy [10], and light-trapping in solar cells [11]. A few nanoloop structures have been designed using the finite-difference time-domain [12] and the finite integration technique [13]. However, these full-wave simulations require a large amount of computational resources as well as time and, furthermore, provide limited intuition into the physical nature of the solution. This paper will provide closed-form analytical expressions for the radiation properties of a nanoloop, which will lead to a more fundamental understanding of such devices and greatly reduced design cycle times.

Early experimental and theoretical results for the far-field radiation of PEC thin-wire circular loops of all sizes have been well documented [14], [15]. More recently, this theory has been extended to include the derivation of exact expressions for the near fields, which can be found in [16] and [17]. The accuracy of these expressions relies on knowledge of the current on the thin-wire loop, which is achieved by considering a Fourier series expansion of the surface current density [18]. Then, the 1-D integral equation (IE) that arises from enforcing the appropriate boundary condition at the surface of the loop can be solved [19]. The problem was revisited for the purpose of analyzing the resonance properties of loops in the context of metamaterials research [20]. This paper was later extended by the same authors to include the analysis of thin-wire nanoloops

Manuscript received May 25, 2016; revised October 18, 2016; accepted October 19, 2016. Date of publication November 1, 2016; date of current version January 2, 2017. This work was supported in part by the Spanish Ministry of Education through the Commission Fulbright Program "Salvador de Madariaga" under Grant PRX14/00320, in part by the Spanish and Andalusian Research Programs under Grant TEC2013-48414-C3-01 and Grant P12-TIC-1442, and in part by the Center for Nanoscale Science, NSF Materials Research Science and Engineering Center, under Award DMR-1420620.

B. Q. Lu, J. Nagar, T. Yue, and D. H. Werner are with the Electrical Engineering Department, The Pennsylvania State University, University Park, PA 16802 USA (e-mail: byl5088@psu.edu; jun16e3@psu.edu; txy143@psu.edu; dhw@psu.edu).

M. F. Pantoja is with the Electrical Engineering Department, University of Granada, 18010 Granada, Spain (e-mail: mario@ugr.es).

Color versions of one or more of the figures in this paper are available online at http://ieeexplore.ieee.org.

Digital Object Identifier 10.1109/TAP.2016.2624150

operating in the infrared and optical regimes [21], [22]. Knowledge of the currents and input impedance facilitates the derivation of exact analytical expressions for the radiation parameters of these antennas. Previous work has presented analytical expressions for radiation properties of plasmonic nanoparticle arrays [23] and nanorods [24]. However, these derivations have proven to be extremely challenging for nanoloop geometries (even thin-wire PEC loops), mainly due to the complex form of the integrals that must be solved [16], [17], [25]–[28]. In this paper, valuable closed-form expressions are derived for the total radiated power, radiation resistance, directivity, and gain of a thin-wire nanoloop antenna. Prior to this work, simple and efficient closed-form expressions for these radiation quantities were not available in the literature.

Section II presents exact expressions for the electromagnetic far-fields radiated by a nanoloop, which are valid from the microwave to optical regimes. Section III validates the resulting analytical expressions by considering two particular cases and comparing the theoretical results with those obtained through the application of full-wave numerical methods. In addition, the differences between the behavior of thin-wire PEC and gold nanoloops are considered. Finally, guidelines for the efficient numerical evaluation of the required integrals (e.g., integrals involving Bessel and Lommel–Weber functions, and Q-type integrals) are provided in the Appendix. It is important to note that the final derived expressions do not involve any integrals and therefore do not require any specialized numerical integration software to implement. In fact, we show in the Appendix that the various power series representations we derive are considerably more efficient than numerical quadrature.

II. Theoretical Formulation

First, we will briefly summarize the classic works by Storer [18] and Wu [19] in which the current on a PEC loop is expressed in terms of a Fourier series. Next, we will discuss how McKinley *et al.* [22] extended this formulation to the optical regime by including the effects of material dispersion and loss. Using these analytical representations together with those derived by Werner [16] for the far-zone electric fields radiated by a thin-wire PEC loop as a starting point, we will derive the first closed-form expressions for the radiated power, radiation efficiency, directivity, and gain associated with thin-wire nanoloops operating in the terahertz, infrared and optical regimes.

Fig. 1 shows the geometry of a thin circular loop with wire radius a and loop radius b. We will start with a Fourier series solution for the current on a PEC loop [18], which can be generalized in terms of resonant modes as [20]

$$I(\varphi) = \sum_{m=-\infty}^{\infty} I_m e^{jm\varphi} = V_0\left[Y_0 + \sum_{m=1}^{\infty} Y_m \cos(m\varphi)\right] \quad (1)$$

where the input impedance for each mode is given by

$$\begin{aligned} Y_0 &= Z_0^{-1} = [j\pi\eta_0 a_0]^{-1} \\ Y_m &= Z_m^{-1} = [j\pi\eta_0 (a_m/2)]^{-1} \end{aligned} \quad (2)$$

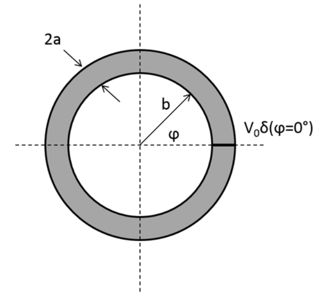

Fig. 1. Geometry of the thin circular loop ($a^2 \ll b^2$). An infinitesimal voltage source with constant voltage V_0 is placed at $\varphi = 0$.

in which η_0 is the characteristic impedance of free space, and the terms a_m are determined from [18], [19]

$$a_m = a_{-m} = k_b\left(\frac{N_{m+1} + N_{m-1}}{2}\right) - \frac{m^2}{k_b}N_m. \quad (3)$$

The variable $k_b = 2\pi b/\lambda$ appearing in (3) is a unit-less quantity that depends on the loop radius. For $m \geq 1$, the auxiliary functions N_m are defined as

$$\begin{aligned} N_m &= N_{-m} = \frac{1}{\pi}\left[K_0\left(\frac{ma}{b}\right) I_0\left(\frac{ma}{b}\right) + C_m\right] \\ &\quad - \frac{1}{2}\int_0^{2k_b} [\Omega_{2m}(x) + jJ_{2m}(x)]\,dx \\ C_m &= \ln(4m) + \gamma - 2\sum_{k=0}^{m-1}\frac{1}{(2k+1)} \end{aligned} \quad (4)$$

where $\gamma \approx 0.5772$ is the Euler–Mascheroni constant and $\Omega_m, J_m, I_0,$ and K_0 are Lommel–Weber functions, Bessel functions of the first kind, and modified Bessel functions of the first and second kind, respectively. For the case where $m = 0$, we have

$$N_0 = \frac{1}{\pi}\ln\left(8\frac{b}{a}\right) - \frac{1}{2}\int_0^{2k_b}[\Omega_0(x) + jJ_0(x)]\,dx. \quad (5)$$

The electric current given by (1) and (2) can be extended into the optical regime by taking into account the lossy and dispersive properties of the constituent materials (e.g., noble metals), an effect captured by the characteristic impedance of the metal, Z_s. The characteristic impedance is not to be confused with the source impedance, often also abbreviated as Z_s. For the case of a cylindrical wire, the characteristic impedance can be expressed in terms of the transverse propagation constant, γ, and the conductivity of the material, σ, in the following form [29], [30]:

$$Z_s = \frac{\gamma}{\sigma}\frac{J_0(\gamma a)}{J_1(\gamma a)} \quad (6)$$

where the propagation constant and the conductivity are related to the refractive index of the material, $\eta = n - j\kappa$, by

$$\gamma = \frac{\omega}{c}\eta \quad (7)$$

$$\sigma = j\omega\epsilon_0(\eta^2 - 1). \quad (8)$$

The refractive index (from the microwave to optical regimes) can be represented by a Drude-like model [3] extended to include critical points of the band transitions as Lorentzian resonances [31], [32]. This leads to a convenient analytical formulation [22]

$$\eta^2 = 1 - \frac{f_0\omega_p^2}{\omega}\left(\frac{1}{\omega - j2\Gamma_0} + \frac{\alpha}{\omega - j2\beta\Gamma_0}\right) + \sum_{m=1}^{M}\frac{f_m\omega_p^2}{2\omega_m}\left(\frac{e^{j\frac{\pi}{\gamma_m}}}{\omega_m - \omega + j\Gamma_m} + \frac{e^{-j\frac{\pi}{\gamma_m}}}{\omega_m + \omega - j\Gamma_m}\right) \tag{9}$$

where M is the number of critical points, ω_p is the plasma frequency, f_m are the quantum probabilities of transition, ω_m are the critical points, Γ_m are the Lorentz broadening terms, and the coefficients α and β are chosen to fit experimental data based on the DC conductivity.

Next, the surface current on the loop (1), (2) can be extended for imperfect conductors by modifying the impedances in the following way, where the prime notation indicates that the characteristic impedance Z_s of the wire has been included:

$$I(\varphi) = V_0\left[Y_0' + \sum_{m=1}^{\infty} Y_m' \cos(m\varphi)\right] \tag{10}$$

where

$$\begin{aligned} Y_0' &= [j\pi\eta_0 a_0 + (b/a) Z_s]^{-1} \\ Y_m' &= [j\pi\eta_0 (a_m/2) + (b/a)(Z_s/2)]^{-1}. \end{aligned} \tag{11}$$

The knowledge of the surface currents given by (10) and (11) enables the derivation of expressions for the far-zone electromagnetic fields and, consequently, the associated far-zone antenna parameters. Hence, the far-zone electric field may be expressed in spherical coordinates (θ, φ) as [16], [17]

$$\begin{aligned} E_\theta &= -\frac{\eta_0 e^{-jk_0 r}\cot\theta}{2r}\sum_{m=1}^{\infty} m j^m I_m \sin(m\varphi) J_m(k_b \sin\theta) \\ E_\varphi &= -\frac{\eta_0 e^{-jk_0 r} k_b}{2r}\sum_{m=0}^{\infty} j^m I_m \cos(m\varphi) J_m'(k_b \sin\theta) \end{aligned} \tag{12}$$

where J_m' is the derivative (with respect to the argument) of the Bessel function of order m, and the modal currents I_m are derived from (10) and (11) as

$$I_m = \frac{D_m V_0}{j\pi\eta_0 a_m + Z_s} = Y_m' V_0 = \left(Z_m'\right)^{-1} V_0 \tag{13}$$

with $D_0 = 1, D_m = 2$ $(m = 1, 2, \ldots)$, while Y_m' and Z_m' are the modal input admittance and impedance, respectively. The computational implementation of (13) requires the solution of certain integrals involving Lommel–Weber and Bessel functions, which are found in (4) and (5). An extended discussion of the procedures and their numerical implementation are provided in Appendices A and B. Now that these fundamental expressions from previous papers have been presented, they are used in the following sections as the basis to derive the first closed-form representations for the radiation properties of a thin-wire nanoloop antenna.

A. Input Impedance, Radiated Power, Radiation Resistance, and Efficiency

In this section, convenient analytical representations for the important parameters which characterize the radiation properties of a loop antenna are derived. The input impedance of the thin-wire loop is directly obtained from (10) as

$$Z_{\text{in}} = \frac{V_0}{I_{\text{in}}} = \left[Y_0' + \sum_{m=1}^{\infty} Y_m'\right]^{-1}. \tag{14}$$

Next, the total radiated power can be determined from (12) by utilizing the following expression:

$$P_r(k_b) = \int_0^{2\pi}\int_0^{\pi} \frac{|E|^2}{2\eta_0} r^2 \sin\theta d\theta d\varphi \tag{15}$$

where $|E|^2 = E_\theta E_\theta^* + E_\varphi E_\varphi^*$. By invoking the orthogonality properties of sinusoidal functions

$$\begin{aligned} \int_0^{2\pi} \sin(m\varphi)\sin(n\varphi)\, d\varphi &= \begin{cases} 0, & m \neq n \\ \pi, & m = n \end{cases} \\ \int_0^{2\pi} \cos(m\varphi)\cos(n\varphi)\, d\varphi &= \begin{cases} 0, & m \neq n \\ \pi, & m = n \end{cases} \end{aligned} \tag{16}$$

the integral (15) can be simplified by means of

$$\begin{aligned} \int_0^{2\pi} E_\theta E_\theta^* d\varphi &= \frac{\pi\eta_0^2\cot^2\theta}{4r^2}\sum_{m=1}^{\infty} m^2 |I_m|^2 J_m^2(k_b \sin\theta) \\ \int_0^{2\pi} E_\varphi E_\varphi^* d\varphi &= \frac{\pi\eta_0^2 k_b^2}{4r^2}\sum_{m=0}^{\infty} |I_m|^2 J_m'^2(k_b \sin\theta). \end{aligned} \tag{17}$$

Hence, by substituting (17) into (15), the total radiated power can be represented as

$$P_r(k_b) = \frac{\eta_0\pi k_b^2}{8}\sum_{m=0}^{\infty}|I_m|^2\left[\int_0^{\pi}\sin\theta J_m'^2(k_b\sin\theta)\, d\theta + \frac{m^2}{k_b^2}\int_0^{\pi}\cos^2\theta\sin^{-1}\theta J_m^2(k_b\sin\theta)\, d\theta\right]. \tag{18}$$

A more compact version of (18) can be derived by considering the Q-type integrals (see [25]–[28] for thin-wire PEC loops), which are defined as

$$Q_{mn}^{(p)}(x) = \int_0^{\frac{\pi}{2}} J_m(x\sin\theta) J_n(x\sin\theta)\sin^p\theta d\theta. \tag{19}$$

Based on (19), a useful recurrence relation can be derived for the case where $n = m$

$$Q_{mm}^{(-1)}(x) = \frac{x^2}{4m^2}\left[Q_{m-1m-1}^{(1)}(x) + 2Q_{m-1m+1}^{(1)}(x) + Q_{m+1m+1}^{(1)}(x)\right]. \tag{20}$$

Next, by making use of (19) and (20), the expression for the total radiated power given in (18) can be simplified to

$$P_r(k_b) = \frac{\eta_0\pi k_b^2}{4}|V_0|^2 T(k_b) \tag{21}$$

where the modal current has been expressed in terms of the driving voltage V_0 and modal admittances Y'_m. The function T can be expressed in terms of Q-type integrals

$$T\,(k_b) = \sum_{m=0}^{\infty} \left|Y'_m\right|^2 \left[\frac{1}{2} Q^{(1)}_{m-1m-1}\,(k_b) + \frac{1}{2} Q^{(1)}_{m+1m+1}\,(k_b) - \frac{m^2}{k_b^2} Q^{(1)}_{mm}\,(k_b)\right]. \tag{22}$$

Details for an efficient and accurate computational implementation for evaluating the Q-type integrals can be found in Appendix C.

The input radiation resistance is defined in [5] in terms of the total radiated power and the input current as

$$R_{\text{rad,in}} = \frac{2P_r\,(k_b)}{|I_{\text{in}}|^2} = \frac{2\,|Z_{\text{in}}|^2\,P_r\,(k_b)}{|V_0|^2}. \tag{23a}$$

This expression can also be rewritten in terms of Q-type integrals and modal admittances by using (21)

$$R_{\text{rad,in}} = \frac{k_b^2 \pi\,\eta_0}{2}\,|Z_{\text{in}}|^2\,T\,(k_b)\,. \tag{23b}$$

An alternate version of radiation resistance defined in [5] is relative to the current maximum and is given by

$$R_{\text{rad}} = \frac{2P_r\,(k_b)}{|I_{\max}|^2}. \tag{24a}$$

Most of the time, the current maximum occurs at the input terminals ($\varphi = 0°$) or at $\varphi = 180°$. For the case of the input terminals, the two definitions for radiation resistance yield identical results. For the case of $\varphi = 180°$, R_{rad} is given by

$$R_{\text{rad}} = \frac{k_b^2 \pi\,\eta_0}{2} \frac{T\,(k_b)}{\left|Y'_0 + \sum_{m=1}^{\infty} (-1)^m Y'_m\right|^2}. \tag{24b}$$

Next, the loss resistance is defined as [27]

$$\begin{aligned} R_{\text{loss}} &= \frac{b}{a} \frac{\operatorname{Re}\,(Z_s)}{|I_{\text{in}}|^2} \frac{1}{2\pi} \int_0^{2\pi} |I\,(\varphi)|^2\,d\varphi \\ &= \operatorname{Re}\,(Z_s)\,\frac{b}{a}\frac{|Z_{\text{in}}|^2}{2}\left[2\left|Y'_0\right|^2 + \sum_{m=1}^{\infty}\left|Y'_m\right|^2\right]. \end{aligned} \tag{25}$$

An expression for the radiation efficiency can be now be derived using (23b) and (25)

$$\begin{aligned} e &= \frac{R_{\text{rad,in}}}{R_{\text{rad,in}} + R_{\text{loss}}} \\ &= \left[1 + \frac{b}{a}\frac{\operatorname{Re}\,(Z_s)}{k_b^2 \pi\,\eta_0 T\,(k_b)}\left(2\left|Y'_0\right|^2 + \sum_{m=1}^{\infty}\left|Y'_m\right|^2\right)\right]^{-1}. \end{aligned} \tag{26}$$

The implementation of the expressions presented in this section requires the truncation of the infinite series of modal impedances. As a general rule, the larger the value of k_b the higher the number of modes would be required to achieve reasonable accuracy. Fig. 2 illustrates this fact by presenting the efficiency of a gold nanoloop with a 600 nm radius (further analyzed in Section III) as the number of modes is increased. Also, we remark that underflow errors can arise for extremely large k_b and modes m, as further explained in the Appendices.

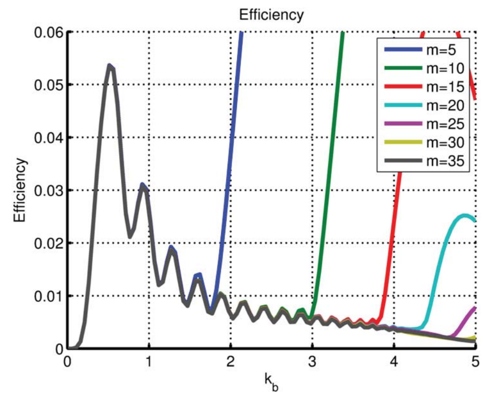

Fig. 2. Efficiency versus k_b for different values of the maximum number of modes considered for a gold nanoloop with circumference $2\pi b = 600$ nm and wire radius $a = b/64.21$ nm ($\Omega = 12$).

B. Radiation Intensity, Directivity, and Gain

The radiation intensity at (θ,φ) can be defined in terms of the normalized far-zone electric fields $E^0_\theta = re^{jk_0 r}E_\theta$, $E^0_\varphi = re^{jk_0 r}E_\varphi$, in the form

$$U\,(\theta,\varphi) = \frac{1}{2\eta_0}\left[\left|E^0_\theta\right|^2 + |E^0_\varphi|^2\right] \tag{27}$$

where from (12)

$$\begin{aligned} |E^0_\theta|^2 &= \frac{|V_0|^2\,\eta_0^2 \cot^2\theta}{4} \times \sum_{m=1}^{\infty}\sum_{n=1}^{\infty}\left[\begin{array}{l} mn\,(-1)^n\,j^{m+n} Y'_m Y'^*_n \sin\,(m\varphi)\,\cdot \\ \sin\,(n\varphi)\,J_m\,(k_b\sin\theta)\,J_n\,(k_b\sin\theta)\end{array}\right] \\ |E^0_\varphi|^2 &= \frac{|V_0|^2\,\eta_0^2 k_b^2}{4} \times \sum_{m=0}^{\infty}\sum_{n=0}^{\infty}\left[\begin{array}{l} (-1)^n\,j^{m+n} Y'_m Y'^*_n \cos\,(m\varphi)\,\cdot \\ \cos\,(n\varphi)\,J'_m\,(k_b\sin\theta)\,J'_n\,(k_b\sin\theta)\end{array}\right]. \end{aligned} \tag{28}$$

Next, an expression for the directivity at (θ,φ) can be found from

$$D\,(\theta,\varphi) = \frac{4\pi\,U\,(\theta,\varphi)}{P_r\,(k_b)} \tag{29}$$

by using expressions (21), (27), and (28). As will be discussed in Section III, convenient expressions for the directivity can be obtained from (29) for some special cases of interest as

$$D\,(0°,0°) = \frac{\left|Y'_1\right|^2}{2T\,(k_b)} \tag{30}$$

$$D\,(90°,0°) = \frac{2}{T\,(k_b)}\sum_{m=0}^{\infty}\sum_{n=0}^{\infty}\left[\begin{array}{l}(-1)^n\,j^{m+n} Y'_m Y'^*_n\cdot \\ J'_m\,(k_b)\,J'_n\,(k_b)\end{array}\right] \tag{31}$$

$$D\,(90°,180°) = \frac{2}{T\,(k_b)}\sum_{m=0}^{\infty}\sum_{n=0}^{\infty}\left[\begin{array}{l}(-1)^m\,j^{m+n} Y'_m Y'^*_n\cdot \\ J'_m\,(k_b)\,J'_n\,(k_b)\end{array}\right]. \tag{32}$$

Finally, the gain of the nanoloop antenna can be expressed in terms of the radiation efficiency and the directivity such

TABLE I
PARAMETERS FOR REFRACTIVE INDEX OF GOLD [26], [27]

Parameter	Value	Parameter	Value
α	1.54	f_2	0.35
β	13.18	ω_2	3.70
f_0	0.37	γ_2	4.00
Ω_0	0.005	Γ_2	1.10
f_1	0.20	f_3	0.60
ω_1	2.62	ω_3	7.00
γ_1	4.00	γ_3	4.00
Γ_1	0.60	Γ_3	2.20
ω_p	9.0		

TABLE II
COMPARISON OF REQUIRED COMPUTATIONAL RESOURCES

Method	Time	Memory
MATLAB	20 seconds	16.7 MB
FEKO	2.1 hours	1.93 GB
CST	2.4 hours	15.9 GB

that

$$\begin{aligned} G(\theta,\varphi) &= eD(\theta,\varphi) \\ &= D(\theta,\varphi) \\ &\quad\times\left[1+\frac{b}{a}\frac{\operatorname{Re}(Z_s)}{k_b^2\pi\eta_0 T(k_b)}\left(2\left|Y_0'\right|^2+\sum_{m=1}^{\infty}\left|Y_m'\right|^2\right)\right]^{-1}. \end{aligned} \tag{33}$$

III. RESULTS

The validation of the analytical equations derived in the previous section will be carried out by considering a gold loop with two different values of circumference, $2\pi b$, namely, 600 nm and 3 μm. The radius of the wire for both models uses the same unit-less thickness measure defined as $\Omega = 2\ln(2\pi b/a) = 12$ (see [20]), which leads to wire radii of 9.3 and 46.7 nm for the 600 nm and 3 μm loop, respectively. The gold material is modeled according to the parameters listed in Table I.

The equations derived in Section II can be implemented by employing software with a powerful symbolic/analytical mathematical engine (e.g., Mathematica), or by applying appropriate numerical methods (e.g., MATLAB). For the second case, useful power series representations are provided in the Appendices for the integrals involving Bessel and Lommel–Weber functions, as well as the Q-type integrals. For further verification, the analytical results were compared to the results from three full-wave frequency-domain tools: 1) the thin-wire IE solver described in [33]; 2) the IE solver of Altair Engineering's FEKO [34]; and 3) the finite-element method solver of CST Microwave Studio [35]. In the computational model for these full-wave solvers, a voltage gap of negligible capacitance was applied as the excitation. Material properties were considered by inserting a table of refractive indices for FEKO and CST, and when appropriate, proper symmetry planes were assigned to speed up the full-wave simulations of the commercial software packages. The expression for input impedance was implemented in MATLAB R2014a using (3)–(6), where the integrals involving Bessel and Lommel–Weber functions were evaluated using exact series representations as discussed in Appendices A and B. A comparison of the computational resources needed for each of the simulation methods considered is provided in Table II. The tests were run on a Dual Intel Xeon Processor with ten cores. FEKO was run in parallel utilizing all ten cores, while the other simulation methods only used a single core. As can be seen, the full-wave simulation methods take more than 2 h to complete, while the analytical solution in MATLAB only takes 20 s. There is also a significant savings in peak memory usage; the full-wave solvers require 2–16 GB and the analytical solution only needs 16.7 MB. The computational resources required to perform the full-wave simulations make experimentation with different nanoantenna geometries and material compositions over a wide frequency range intractable. Furthermore, this problem is exacerbated when dealing with nanoloop arrays, a popular configuration for solar cells [11], and applications requiring extremely directive patterns [9]. An analytical solution for the mutual admittances of loop antennas in the array environment is beyond the scope of this paper but will be considered in a future work. While the full-wave solvers enable simulation of arbitrary geometries,

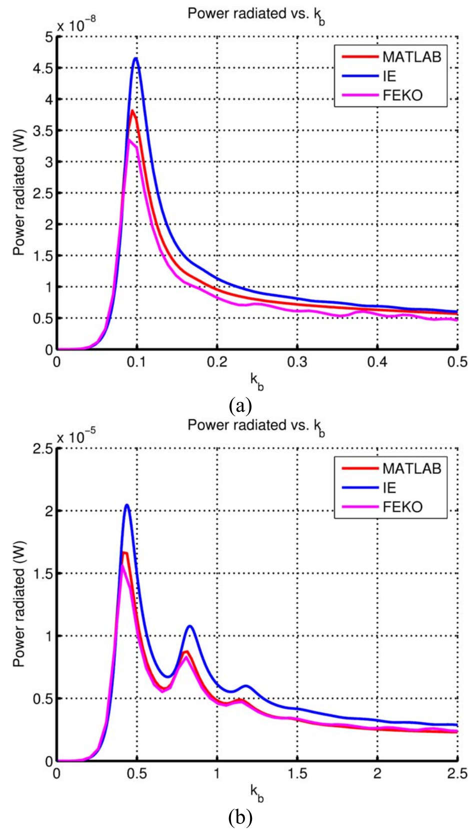

Fig. 3. Comparison of the total power radiated versus k_b evaluated using three different simulation techniques for (a) 600 nm circumference and (b) 3000 nm circumference gold nanoloops.

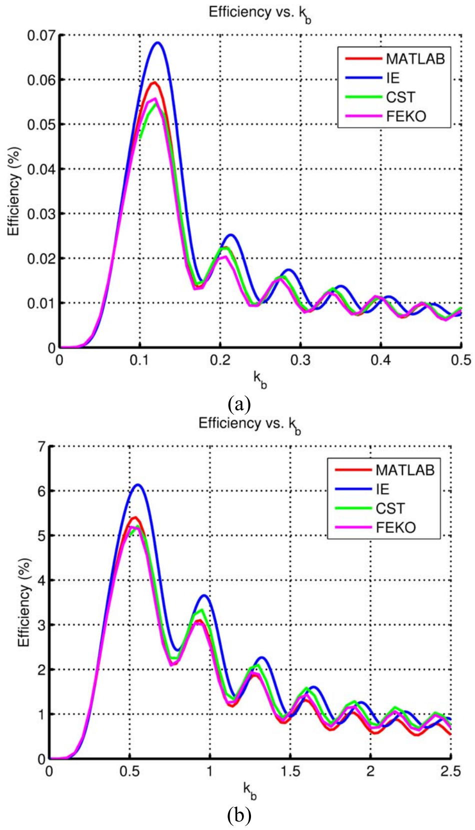

Fig. 4. Comparison of efficiency versus k_b evaluated using four different simulation techniques for (a) 600 nm circumference and (b) 3000 nm circumference gold nanoloops.

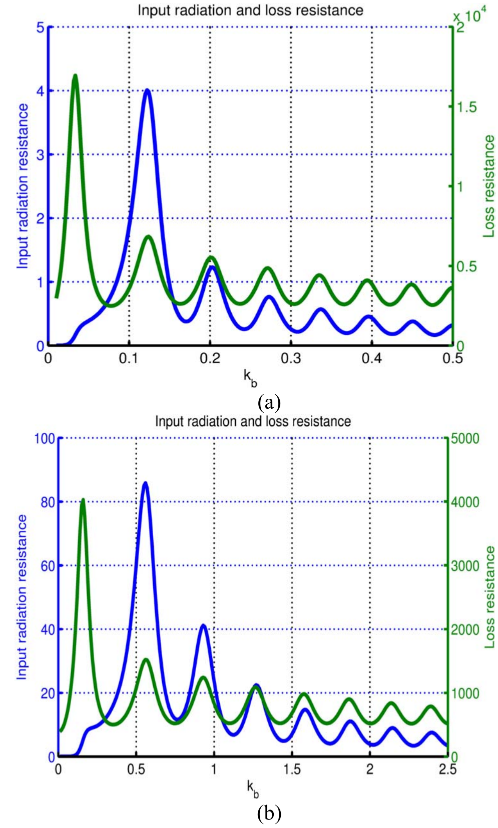

Fig. 6. Input radiation and loss resistance in Ohms versus k_b for (a) 600 nm circumference and (b) 3000 nm circumference gold nanoloops.

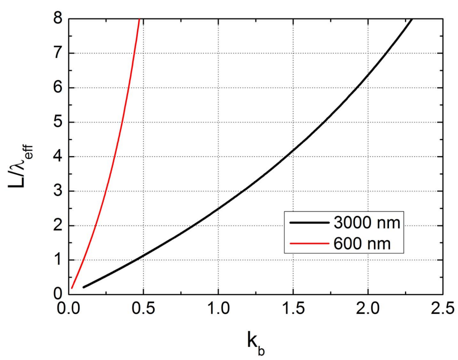

Fig. 5. Electrical size in terms of effective wavelength versus k_b for the two thin-wire gold nanoloops.

the closed-form expressions derived here allow for extremely rapid simulation of nanoloops and, furthermore, they provide insight into the radiation mechanisms of these structures. For example, by examining the complex coefficients for each term in the summations of (28), the individual modal contributions to the theta and phi components of the far-zone electric field can be isolated and analyzed.

Figs. 3 and 4 show plots of the total radiated power and efficiency, respectively, for the two example cases of nanoloops under consideration. The analytical results were obtained by using (21) and (26), with comparisons made to full-wave simulations. As indicated in Fig. 2, approximately 35 modes were enough to accurately determine the efficiency out to k_b= 5. Hence, 35 modes will be utilized for all analytical results presented herein. The analytical and full-wave methods are found to be in relatively good agreement, with some larger discrepancy exhibited by the IE-based solution. This is mainly due to the piecewise approximation employed to describe the curved geometry of the nanoloop, which results in a slightly higher calculated radiated power and efficiency than the actual values [36].

To further analyze the results, we consider the effective wavelength concept presented in [10] and reproduced in Fig. 5. In essence, the effective wavelength accounts for the propagation of the plasmonic mode (i.e., the TM_0 mode). Hence, the physical phenomena in the infrared/optical regimes can be described by applying scale factors that correspond to the effective wavelength. The maxima of the radiated power and the efficiency are achieved at the resonances, which are situated along the L/λ_{eff} curves depicted in Fig. 5, spaced apart by approximately integer values of L/λ_{eff}. This result explains why there are only six peaks for the 600 nm loop in the range from 0 to $0.5k_b$, and seven peaks for the 3000 nm loop in the range from 0 to $2.5k_b$. Similar to the behavior of microwave loop antennas [5], the maximum values of the total radiated power are reached at the first resonant mode, while the successive maxima will decrease for higher frequencies. In addition, an increase in size leads to higher values of the radiated power and the efficiency. To gain more insight into the

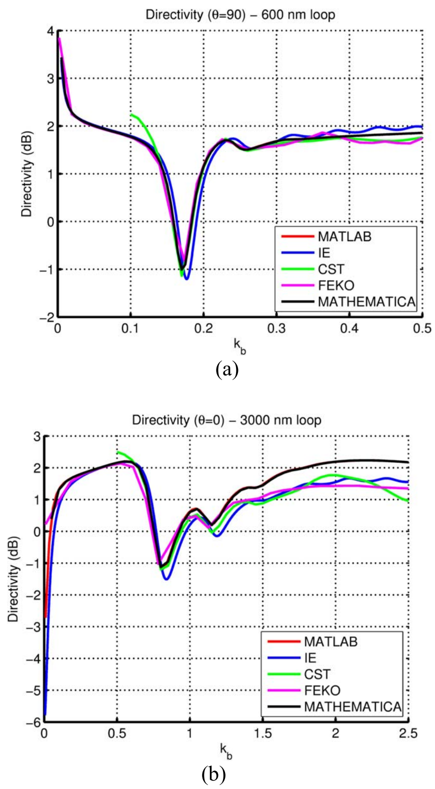

Fig. 7. (a) Directivity of the 600 nm loop evaluated at $(\theta, \varphi) = (90°, 0°)$. (b) Directivity of the 3000 nm loop evaluated at $(\theta, \varphi) = (0°, 0°)$.

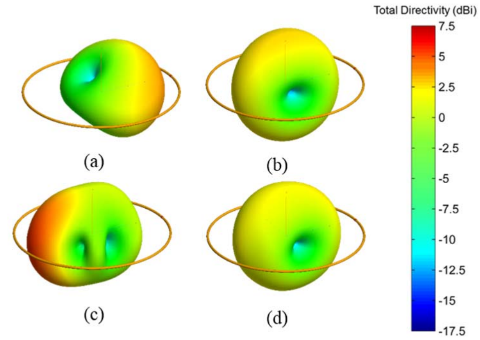

Fig. 8. Directivity corresponding to a 3000 nm gold loop as computed by FEKO for k_b values of (a) 0.01, (b) 0.5, (c) 1.1, and (d) 2.5.

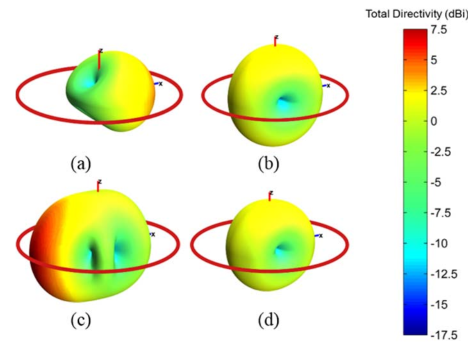

Fig. 9. Directivity corresponding to a 3000 nm gold loop as computed by MATLAB for k_b values of (a) 0.01, (b) 0.5, (c) 1.1, and (d) 2.5.

efficiency, the expressions for the input radiation resistance and loss resistance given in (23b) and (25), respectively, are plotted in Fig. 6. The magnitude of the input radiation resistance for the 600 nm loop attains a maximum value of only 4 Ω. This, coupled with the low input admittance and driving current, result in the low total radiated power indicated in Fig. 3(a). In addition to this, the loss resistance is extremely high, leading to a low efficiency of only 0.07% as determined from Fig. 4(a). For the 3000 nm case, the input radiation resistance reaches about 80 Ω and the corresponding efficiency is above 6%. The radiation resistance relative to the maximum current given in (24a) follows those of the input radiation resistance of Fig. 6 very closely, except the maximum value for the 600 nm loop is now about 2 Ω and the max for the 3000 nm loop is about 40 Ω.

To validate the expressions given in (29)–(32) for directivity, they were evaluated and their results compared with full-wave solvers. Fig. 7 shows a comparison of the directivity for the 600 nm loop evaluated at $(\theta, \varphi) = (90°, 0°)$ and the 3000 nm loop evaluated at $(\theta, \varphi) = (0°, 0°)$. The numerical implementations in MATLAB and Mathematica yield essentially equivalent results, while providing reasonable agreement with the full-wave solvers.

Next, FEKO was used to generate 3-D directivity plots for the 3000 nm loop antenna with $k_b = 0.01$, 0.5, 1.1, and 2.5 (similar radiation patterns were observed for the 600 nm loop). These results are shown in Fig. 8 when the material is gold and in Fig. 10 when PEC wire is assumed. For further validation of the analytical derivation, the 3-D radiation patterns as computed by MATLAB are shown in Fig. 9 for gold. Comparing Fig. 8 with Fig. 9 demonstrates that the patterns are nearly identical. A PEC loop for $k_b = 0.01$ exhibits a far-field pattern which is similar to that of a magnetic dipole, omnidirectional in the plane of the loop with nulls in the normal directions, as shown in Fig. 10(a). However, the nanoloop for $k_b = 0.01$ exhibits a directive pattern with a peak of 6 dBi, as shown in Fig. 8(a). The losses in the gold cause the azimuthal symmetry of the current distribution to be broken, resulting in constructive interference for the case where $(\theta, \varphi) = (90°, 0°)$. For the PEC case, as frequency increases, the peak directivity shifts to the normal direction $(\theta, \varphi) = (0°, 180°)$ at around $k_b = 1.1$, as shown in Fig. 10(c) [5]. This behavior can also be seen in the nanoloop, but it occurs instead around $k_b = 0.5$, as shown in Fig. 8(b). However, at around $k_b = 0.85$ the peak then shifts to $(\theta, \varphi) = (90°, 180°)$ with the maximum directivity of 7.5 dBi occurring at $k_b = 1.1$, as shown in Fig. 8(c). This is again due to the attenuation of the currents, where at this frequency the moderate losses lead to extremely strong constructive interference. Finally, at around $k_b = 2.5$, the pattern again becomes omnidirectional in the *xz* plane as shown in Fig. 8(d). In this regime, only the part of the nanoloop close to the source is radiating, and thus a radiation pattern resembling a nanodipole appears. This is in stark contrast to the behavior of PEC loops, where the far-field pattern starts to exhibit multiple lobes at around $k_b = 2.0$. As k_b is increased above this for a PEC loop, the far-field

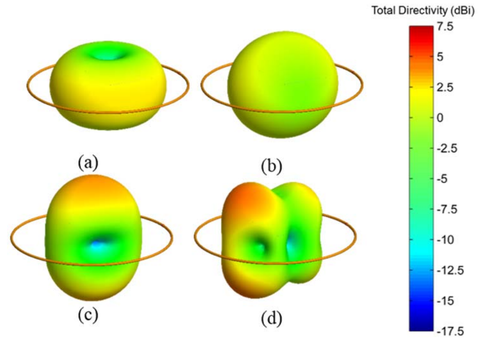

Fig. 10. Directivity corresponding to a 3000 nm PEC loop as computed by FEKO for k_b values of (a) 0.01, (b) 0.5, (c) 1.1, and (d) 2.5.

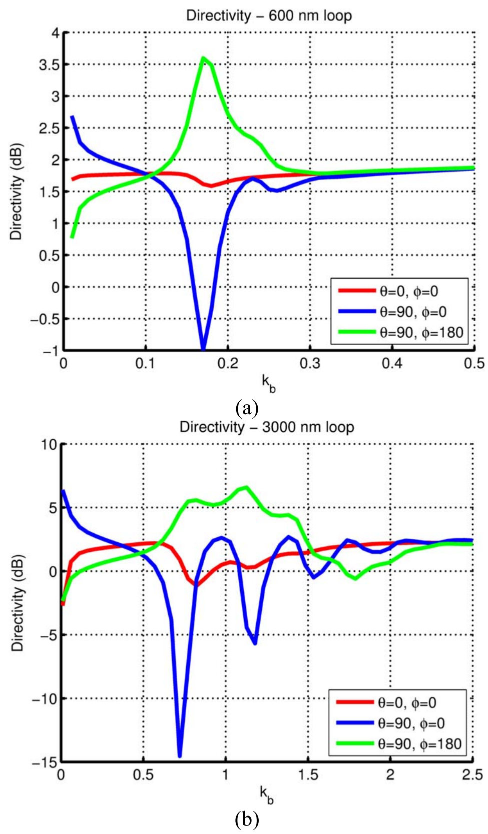

Fig. 11. Directivity of (a) 600 nm loop and (b) 3000 nm loop corresponding to angles of $(\theta, \varphi) = (0°, 0°)$, $(\theta, \varphi) = (90°, 0°)$, and $(\theta, \varphi) = (90°, 180°)$.

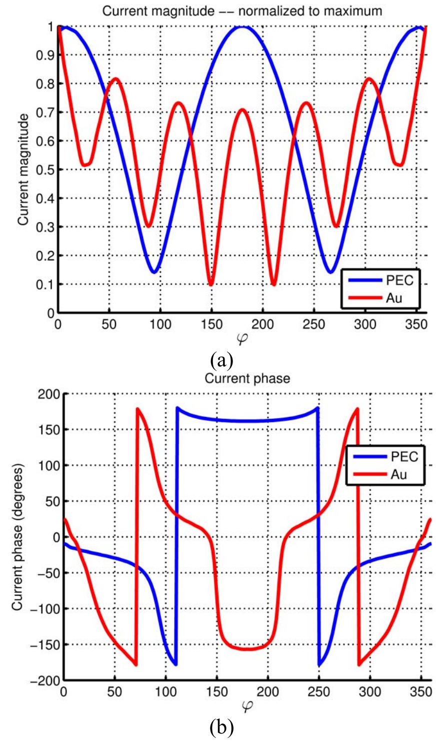

Fig. 12. Comparison between the 3000 nm PEC and gold nanoloop for $k_b = 1.11$. (a) Current magnitude. (b) Current phase.

pattern becomes increasingly more complex, with the number of lobes increasing, as shown in Fig. 10(d) for $k_b = 2.5$. It is important to note that these trends with respect to k_b apply for any circumference in the PEC case but not for the nanoloop. The behavior of the nanoloop is heavily dependent on the circumference and constituent material properties.

To study these trends more thoroughly, the directivity expressions given in (30)–(32) were used to generate the results shown in Fig. 11 for the three angles of interest. For the 600 nm loop, the largest directivities occur at $(\theta, \varphi) = (90°, 0°)$ around $k_b = 0.01$, and at $(\theta, \varphi) = (90°, 180°)$ near $k_b = 0.175$. Above $k_b = 0.175$, the pattern is omnidirectional in the xz plane and remains that way as the frequency increases. The directivity in the yz plane remains low for all frequencies, because of the symmetry and low magnitudes of the currents in that plane (around $\varphi = 90°$ and $\varphi = 270°$). For the 3000 nm loop, the directivity versus frequency for all three directions has a similar behavior to that of the 600 nm loop; however, there are more ripples due to the existence of higher order modes in the currents.

Interestingly, superdirectivity is achieved along $(\theta, \varphi) = (90°, 180°)$ over a broadband for the 3000 nm loop. This phenomenon does not occur for PEC loops and is a direct consequence of the optical properties of gold, which causes the currents around the nanoloop to undergo attenuation. It is well-documented that superdirectivity along the endfire direction can be achieved when two closely spaced PEC dipoles in a linear array are excited with normalized magnitudes of 1 V and approximately 0.7 V along with a phase difference of approximately 180° [37]. An examination of the current distribution shows that this condition arises naturally on the 3000 nm nanoloop over a relatively broad frequency range. Fig. 12 shows a comparison of the current magnitude and the current phase for the 3000 nm PEC and gold nanoloops at $k_b = 1.11$. As can be seen, the conditions for superdirectivity only occur for the lossy gold loop. This surprising behavior is easily and efficiently predicted using (32) and only occurs for nanoloops of a specific size and material composition. As far as the authors know, this phenomenon has not been previously discovered. This is most likely because full-wave solvers require too much time, while the closed-form expressions provided in this paper allow for rapid experimentation with different geometries and material properties.

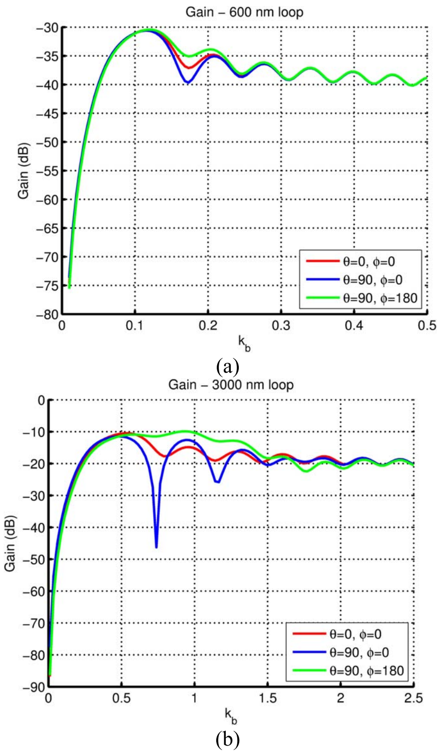

Fig. 13. Gain of (a) 600 nm loop and (b) 3000 nm loop corresponding to angles of $(\theta, \varphi) = (0°, 0°)$, $(\theta, \varphi) = (90°, 0°)$, and $(\theta, \varphi) = (90°, 180°)$.

Finally, Fig. 13 shows the gain as defined in (33) for the three directions under consideration. As expected, the gain is much lower for the 600 nm loop since it corresponds to an electrically smaller antenna. The gain tends to decrease as the frequency increases, which is a consequence of the decreasing efficiency depicted in Fig. 4. Also, it is noteworthy that for the 3000 nm case, the maximum of the gain as well as directivity appears for $k_b \approx 1$ at $(\theta, \varphi) = (90°, 180°)$. Fig. 5 shows that for the 3000 nm loop, these frequencies correspond to $L/\lambda_{\text{eff}} \approx 2.5$ (i.e, approximately the third resonance of the nanoloop). These analytical expressions allow for rapid design cycles by enabling the designer to analyze trends quickly and efficiently. In microwave applications, most designs operate at the first resonance ($L/\lambda_{\text{eff}} \approx 0.5$), but this result implies that nanoloops could be used at higher order resonances where the pattern is more directive and the gain is larger.

IV. Conclusion

Computationally efficient closed-form expressions for the radiation properties of lossy nanoloops which are valid in the terahertz, infrared and optical regimes have been presented in this paper. In particular, analytic expressions are derived for the far-zone radiated electric fields, total radiated power, radiation resistance, directivity, and gain. These expressions are derived by extending the formulation for thin-wire PEC loops to include the effects of dispersion and loss. The closed-form expressions for a gold nanoloop are validated by comparison with full-wave simulations based on several different computational electromagnetics techniques. The full-wave solvers require more than 2 h and 2–16 GB of memory, while the analytical solution as implemented in MATLAB requires only 20 s and 16.7 MB of memory. Additionally, some useful guidelines for computing the required integrals associated with the Bessel and Lommel–Weber functions, along with the Q-type integrals, have been provided in the Appendices.

Appendix A
Calculation of the Integral of the Bessel Function

Integration of the Bessel functions of integer order is required to calculate the coefficients of the modal impedances as described by (4) and (5). This can be performed numerically using the *integral* routine in MATLAB which employs global adaptive quadrature techniques, a method of approximating the integral by calculating areas over adaptively refined intervals [38].

Alternatively, the integral can be accurately calculated using a power series representation. The Bessel function is expressed in the form [39], [40]

$$J_{2m}(x) = \sum_{n=0}^{\infty} \frac{(-1)^n}{n!\,(2m+n)\,!} \left(\frac{x}{2}\right)^{2n+2m} \tag{34}$$

which leads to the result

$$\int_0^{2k_b} J_{2m}(x)\,dx = 2\sum_{n=0}^{\infty} \frac{(-1)^n\,(k_b)^{2n+2m+1}}{n!\,(2m+n)\,!\,(2n+2m+1)}. \tag{35}$$

Another useful representation, especially for larger arguments, can be employed for which the definite integral of a Bessel function is expressed in terms of a series of Bessel functions [39], [40]

$$\int_0^{2k_b} J_{2m}(x)\,dx = 2\sum_{k=0}^{\infty} J_{2m+2k+1}(2k_b). \tag{36}$$

A third formulation can be determined by using generalized hypergeometric functions [41], which are the solutions to the hypergeometric or Gauss's equation, and defined as

$$pFq\left(\begin{matrix} a_1, a_2, \ldots, a_p \\ b_1, b_2, \ldots, b_q \end{matrix}; z\right) = \sum_{k=0}^{\infty} \frac{(a_1)_k \cdots (a_p)_k}{(b_1)_k \cdots (b_q)_k} \frac{z^k}{k!} \tag{37}$$

where $(\ )_k$ denotes the Pochhammer symbol, which is defined as

$$(q)_n = \frac{\Gamma(q+n)}{\Gamma(q)} = \begin{cases} 1, & n = 0 \\ q\,(q+1)\cdots(q+n-1)\,, & n > 0. \end{cases} \tag{38}$$

Bessel functions, along with many other special functions, can be expressed in terms of generalized hypergeometric functions. For example

$$J_{2m}(z) = \frac{z^{2m}}{4^m\,\Gamma(2m+1)}\,{}_0F_1\left(;2m+1;-\frac{z^2}{4}\right). \tag{39}$$

By applying the substitution $u = -(1/4)z^2$, and the integration identity [40]

$$\int z^{\alpha-1}\,{}_0F_1(;b;z)\,dz = z^{\alpha}\frac{\Gamma(\alpha)}{\Gamma(\alpha+1)}\,{}_1F_2(\alpha;b,\alpha+1;z) \tag{40}$$

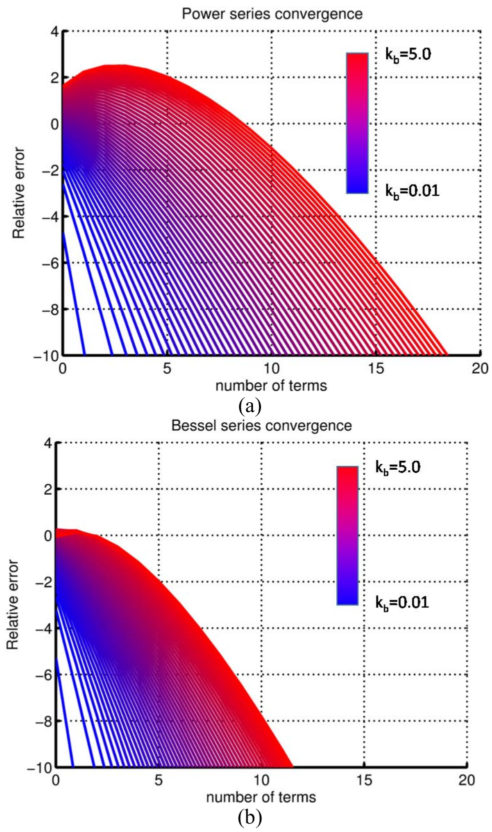

Fig. 14. Logarithm (base 10) of the relative error versus number of terms for the integral of the Bessel function with $m = 1$ using (a) power series (35) and (b) Bessel series (36) representations. The error is computed relative to (41), which involves the confluent hypergeometric function. The parameter k_b increases from 0.01 to 5.0 as the color of the curve varies from blue to red.

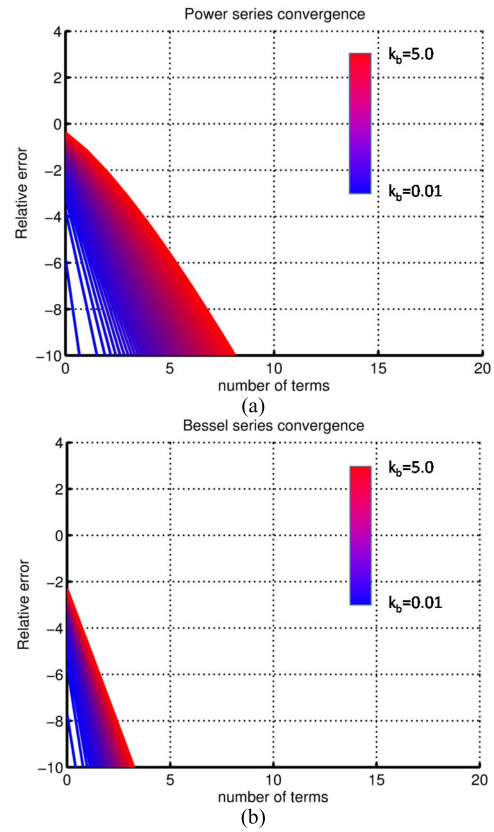

Fig. 15. Logarithm (base 10) of the relative error versus number of terms for the integral of the Bessel function for $m = 35$, using (a) power series (35) and (b) Bessel series (36) representations. The error is computed relative to (41), which involves the confluent hypergeometric function. The parameter k_b increases from 0.01 to 5.0 as the color of the curve varies from blue to red.

the integral in (35) may be written as

$$\int_0^{2k_b} J_{2m}(z)\,dz = \frac{2k_b^{2m+1}}{(2m+1)\,!}\,{}_1F_2\left(m+\frac{1}{2};\,2m+1, m+\frac{3}{2}; -k_b^2\right). \tag{41}$$

Note that it can be shown that (35) and (41) are mathematically equivalent based on the definition of the hypergeometric functions. A robust numerical technique implemented in Mathematica for evaluating the generalized hypergeometric function of the form contained in (41) is discussed in [40] and source code can be found in [43]. An efficient calculation of the Bessel functions in (36) is implemented in MATLAB R2014a [44]. These expressions, along with the power series representation of (35) will be compared in terms of their convergence properties and computation times.

When considering the integration of Bessel functions of low order m, the series of (35) converges rapidly for small arguments. However, for larger values of k_b, the number of terms required to achieve convergence dramatically increases due to the fact that the summation is not monotonically decreasing. Alternatively, the series representation involving Bessel functions (36) converges much quicker for large k_b. This is illustrated in Fig. 14(a) and (b), which show the logarithm (base 10) of the relative error versus the number of terms in the series expansions for m= 1 using (35) and (36). The relative error is defined as $|v - v_{\mathrm{approx}}/v|$ where v is the exact value as computed by the hypergeometric generalized functions or numerical quadrature as specified in the caption and v_{approx} is the approximate series representation.

In practice, the range of k_b is bounded for a goal of an absolute accuracy A and a fixed number of terms n in the power series representation (35), where the absolute accuracy is the difference between the exact value and the series approximation. Performing a ratio test on the series, the maximum value of k_b which can be computed accurately in the calculation of the integral of the Bessel function of order m is

$$k_b < \sqrt{A\frac{(n+1)(2m+2n+3)(2m+n+1)}{(2m+2n+1)}}. \tag{42}$$

This shows why more terms are required for a given accuracy as k_b increases. For large m, a comparison between the two series representations is illustrated in Fig. 15, which considers the case of $m = 35$. Both series representations provide accurate results by just considering a small number of terms, but the power series (35) does not seem to converge better for small arguments k_b, as would be expected of a typical power series, and (36) converges quicker for all arguments. The reason for this is that the built-in numerical routines in MATLAB, which were employed to calculate the Bessel func-

TABLE III
TIMING ESTIMATES FOR BESSEL INTEGRAL EVALUATION

k_b	Time (ms) Power Series	Time (ms) Bessel Series	Time (ms) Quadrature	Time (ms) Mathematica
0.1	0.60	0.017	0.82	0.28
1.0	0.60	0.017	0.82	0.31
2.5	0.60	0.041	0.89	0.35
5.0	0.60	0.046	0.91	0.46

tions, include a combination of extremely efficient algorithms that are selected based on the values of the argument and order [44]. For values of m greater than 35 and k_b greater than 5, the Bessel function calculations can yield underflow errors, a condition where the true value of an operation is smaller in magnitude than the smallest representable floating point number [44]. However, most nanoloops have extremely low efficiencies for k_b greater than 5, so this condition will not be encountered in such cases.

Finally, Table III shows a comparison of the time taken to calculate the integral of the Bessel function for the $m = 1$ case using: 1) the power series representation (35); 2) the Bessel series representation (36); 3) numerical quadrature; and 4) the result (41) in terms of hypergeometric generalized functions (computed in Mathematica 10). For the series representations, 20 terms are considered since this resulted in a relative error of less than 10^{-10} for all k_b. Similarly, the numerical quadrature was computed to a relative error of 10^{-10}. Each calculation was performed 10 000 times and averaged to smooth out any computational noise. For increasing k_b, the time required remains constant for the power series representation since a constant number of terms was used for all cases and the calculations performed remain invariant. It can be seen that numerical quadrature is inefficient and the time taken increases with k_b since more subintervals are required to achieve the desired accuracy. On the other hand, solutions based on built-in functions (i.e., Bessel and generalized hypergeometric functions) are more efficient than the power series and quadrature methods, with the Bessel series being by far the most efficient. The main reason for this is that efficient algorithms for these functions have been studied extensively [43], especially for Bessel functions [44]. However, the time taken increases with increasing k_b due to the underlying choices made between the different algorithms, which is dependent on the order and argument.

APPENDIX B
CALCULATION OF THE INTEGRAL OF THE LOMMEL–WEBER FUNCTION

In addition to the integrals of the Bessel functions, the expressions (4) and (5) also contain integrals of Lommel–Weber functions. Similar to Appendix A, a power series representation and an analytical form in terms of hypergeometric functions will be presented and compared.

The starting point for this derivation is the following power series representation of the Lommel–Weber function which is valid for integer values of m and n:

$$\Omega_{2m}(x) = \sum_{n=0}^{\infty} \frac{(-1)^{n+m}}{\Gamma(n+m+3/2)\,\Gamma(n-m+3/2)} \left(\frac{x}{2}\right)^{2n+1}. \tag{43}$$

The required integral of the Lommel–Weber function may now be evaluated using (43), which leads to the result

$$\int_0^{2k_b} \Omega_{2m}(x)\,dx = \sum_{n=0}^{\infty} \frac{(-1)^{n+m}}{\Gamma(n+m+3/2)\,\Gamma(n-m+3/2)} \times \frac{k_b^{2n+2}}{(n+1)}. \tag{44}$$

Next, a useful analytical form of this integral in terms of hypergeometric functions will be derived. For this development, we note that the Lommel–Weber function for an even integer order can be expressed as

$$\Omega_{2m}(z) = \frac{2}{\pi} \frac{z\,{}_1F_2[1; \frac{1}{2}(-2m+3), \frac{1}{2}(2m+3); -\frac{1}{4}z^2]}{(1-2m)(1+2m)}. \tag{45}$$

By applying the substitution $u = -\frac{1}{4}z^2$, and the integration identity [39]

$$\int z^{\alpha-1}\,{}_1F_2\left[1; -m+\frac{3}{2}, m+\frac{3}{2}; z\right] dz = \frac{z^{\alpha}}{\alpha}\,{}_2F_3\left[\alpha, 1; \alpha+1, -m+\frac{3}{2}, m+\frac{3}{2}; z\right] \tag{46}$$

it can be shown that

$$\int_0^{2k_b} \Omega_{2m}(z)dz = -\frac{4k_b^2\,{}_2F_3\left[1, 1; 2, -m+\frac{3}{2}, m+\frac{3}{2}; -k_b^2\right]}{\pi(2m-1)(2m+1)}. \tag{47}$$

Note that (44) and (47) are mathematically identical. The hypergeometric function that appears in (47) may be computed efficiently and accurately by exploiting the available libraries of built-in functions in Mathematica.

The relative error of the power series approximation follows similar trends to the results shown in Fig. 15(a) and (b) for small and large m, respectively. In particular, for low order m and small values of k_b just a few terms in the series are required to achieve a given accuracy. Again, the more accurate answer was considered to be the result produced by (47), where the evaluation of the hypergeometric function was computed by Mathematica. This approach is also more efficient in terms of computational time than the power series representation of (44).

APPENDIX C
CALCULATION OF THE Q-TYPE INTEGRAL

The numerical implementation of the Q-type integral of (19) is considered next. In terms of a power series representation, the $Q_{nn}^{(1)}$ integral can be calculated as [20]

$$Q_{nn}^{(1)}(k_b) = \sum_{l=0}^{\infty} (-1)^l B_{nn,l} W_{2n+2l+s} \left(\frac{k_b}{2}\right)^{2n+2l} \tag{48}$$

with

$$B_{nn,l} = \frac{\Gamma(2n+2l+1)}{\Gamma(l+1)\left[\Gamma(n+l+1)\right]^2 \Gamma(2n+l+1)} \tag{49}$$

and where

$$\begin{aligned} W_{2n+2l+s} &= \int_0^{\frac{\pi}{2}} \sin^{2n+2l+s} \theta d\theta \\ &= \frac{\pi\,\Gamma(2n+2l+s+1)}{2^{2n+2l+s+1}\left[\Gamma\left(n+l+\frac{s}{2}+1\right)\right]^2} \end{aligned} \tag{50}$$

are known as Wallis integrals [45].

An alternative series representation in terms of Bessel functions can also be derived. Starting with the integral form of $Q_{nn}^{(1)}$, the following series solution can be obtained:

$$\begin{aligned} Q_{nn}^{(1)}(k_b) &= \int_0^{\frac{\pi}{2}} J_n^2(k_b \sin\theta)\sin(\theta)\,d\theta \\ &= \frac{1}{k_b}\sum_{k=0}^{\infty} J_{2n+2k+1}(2k_b). \end{aligned} \tag{51}$$

The derivation of (51) involves the following definite integral [38]:

$$\int_0^a J_v(x)\,dx = 2\sum_{k=0}^{\infty} J_{v+2k+1}(a). \tag{52}$$

In this case, the error computed was relative to numerical quadrature with an extremely small tolerance. When comparing the convergence of the power series (48) and the Bessel series (52), the results are very similar to Fig. 14 for the $m = 1$ case. The conclusions are very similar to those of Appendix A, with the Bessel series being more computationally efficient, especially for large values of k_b. For larger values of m, the required number of terms in the series for a fixed accuracy is reduced, similar to the results shown in Fig. 15.

Acknowledgment

The authors would like to thank Dr. A. F. McKinley for valuable assistance in preparing the MATLAB codes used in this paper. They would also like to thank Dr. A. Panaretos for helpful discussions.

References

[1] J. Schulte, Ed., *Nanotechnology: Global Strategies, Industry Trends and Applications*. London, U.K.: Wiley, 2005.

[2] P. Biagioni, J.-S. Huang, and B. Hecht, "Nanoantennas for visible and infrared radiation," *Rep. Prog. Phys.*, vol. 75, no. 2, p. 024402, Jan. 2012.

[3] P. B. Johnson and R. W. Christy, "Optical constants of the noble metals," *Phys. Rev. B*, vol. 6, no. 12, pp. 4370–4379, Dec. 1972.

[4] L. Novotny and B. Hecht, *Principles of Nano-Optics*. Cambridge, U.K.: Cambridge Univ. Press, 2012.

[5] C. A. Balanis, *Antenna Theory*. New York, NY, USA: Wiley, 1997.

[6] P. Mühlschlegel, H.-J. Eisler, O. J. F. Martin, B. Hecht, and D. W. Pohl, "Resonant optical antennas," *Science*, vol. 308, no. 5728, pp. 1607–1609, Jun. 2005.

[7] P. J. Schuck, D. P. Fromm, A. Sundaramurthy, G. S. Kino, and W. E. Moerner, "Improving the mismatch between light and nanoscale objects with gold bowtie nanoantennas," *Phys. Rev. Lett.*, vol. 94, p. 017402, Jan. 2005.

[8] G. S. Smith, "Loop antennas," in *Antenna Engineering Handbook*, R. Johnson, Ed. New York, NY, USA: McGraw-Hill, 1993.

[9] D. Ahmadian, C. Ghobadi, and J. Nourinia, "Ultra-compact two-dimensional plasmonic nano-ring antenna array for sensing applications," *Opt. Quantum Electron.*, vol. 46, no. 9, pp. 1097–1106, 2014.

[10] D. Etezadi, A. E. Cetin, and A. H. Altug, "Plasmonic nanoantennas on nanopedestals for ultra-sensitive vibrational IR-spectroscopy," in *Proc. Conf. Lasers Electro-Opt. (CLEO)*, San Jose, CA, USA, May 2015, pp. 1–2.

[11] A. F. McKinley, T. P. White, and K. R. Catchpole, "Designing nanoloop antenna arrays for light-trapping in solar cells," in *Proc. Photovolt. Specialists Conf. (PVSC)*, Jun. 2013, pp. 1894–1896.

[12] A. Ahmadi and H. Mosallaei, "Plasmonic nanoloop array antenna," *Opt. Lett.*, vol. 35, no. 21, pp. 3706–3708, 2010.

[13] A. Locatelli, "Peculiar properties of loop nanoantennas," *IEEE Photon. J.*, vol. 3, no. 5, pp. 845–853, Oct. 2011.

[14] G. Glinski, "Note on circular loop antennas with non-uniform current distribution," *J. App. Phys.*, vol. 18, no. 7, pp. 638–644, 1947.

[15] B. R. Rao, "Far field of large circular loop antennas: Theoretical and experimental results," *IEEE Trans. Antennas Propag.*, vol. 8, no. 4, pp. 439–441, Jul. 1960.

[16] D. H. Werner, "An exact integration procedure for vector potentials of thin circular loop antennas," *IEEE Trans. Antennas Propag.*, vol. 44, no. 2, pp. 157–165, Feb. 1996.

[17] D. H. Werner, "Lommel expansions in electromagnetics," in *Frontiers in Electromagnetics*, D. H. Werner and R. Mittra, Eds. Hoboken, NJ, USA: Wiley, 2000.

[18] J. E. Storer, "Impedance of thin-wire loop antennas," *Trans. Amer. Inst. Electr. Eng. I, Commun. Electron.*, vol. 75, no. 5, pp. 606–619, Nov. 1956.

[19] T. T. Wu, "Theory of the thin circular loop antenna," *J. Math. Phys.*, vol. 3, no. 6, pp. 1301–1304, Nov./Dec. 1962.

[20] A. F. McKinley, T. P. White, I. S. Maksymov, and K. R. Catchpole, "The analytical basis for the resonances and anti-resonances of loop antennas and meta-material ring resonators," *J. Appl. Phys.*, vol. 112, no. 9, p. 094911, 2012.

[21] L. Novotny, "Efficient wavelength scaling for optical antennas," *Phys. Rev. Lett.*, vol. 98, no. 26, p. 266802, 2007.

[22] A. F. McKinley, T. P. White, and K. R. Catchpole, "Theory of the circular closed loop antenna in the terahertz, infrared and optical regions," *J. Appl. Phys.*, vol. 114, no. 4, p. 044317, 2013.

[23] A. Alù, "Optical leaky-wave nanoantenna: Complex modes along linear arrays of plasmonic nanoparticles," in *Proc. URSI Int. Symp. Electromagn. Theory (EMTS)*, Berlin, Germany, Aug. 2010, pp. 962–965.

[24] L. Peng and N. A. Mortensen, "Plasmonic-cavity model for radiating nano-rod antennas," *Sci. Rep.*, vol. 4, no. 3825, pp. 1–6, 2014.

[25] S. V. Savov, "An efficient solution of a class of integrals arising in antenna theory," *IEEE Antennas Propag. Mag.*, vol. 44, no. 5, pp. 98–101, Oct. 2002.

[26] J. D. Mahony, "A comment on *Q*-type integrals and their use in expressions for radiated power," *IEEE Antennas Propag. Mag.*, vol. 45, no. 3, pp. 127–128, Jun. 2003.

[27] S. V. Savov, "A comment on the radiation resistance," *IEEE Antennas Propag. Mag.*, vol. 45, no. 3, p. 129, Jun. 2003.

[28] J. D. Mahony, "Circular microstrip-patch directivity revisited: An easily computable exact expression," *IEEE Antennas Propag. Mag.*, vol. 45, no. 1, pp. 120–122, Feb. 2003.

[29] J. A. Stratton, *Electromagnetic Theory*. New York, NY, USA: McGraw-Hill, 1941.

[30] G. W. Hanson, "Radiation efficiency of nano-radius dipole antennas in the microwave and far-infrared regimes," *IEEE Antennas Propag. Mag.*, vol. 50, no. 3, pp. 66–77, Jun. 2008.

[31] P. G. Etchegoin, E. C. L. Ru, and M. Meyer, "An analytic model for the optical properties of gold," *J. Chem. Phys.*, vol. 125, no. 16, p. 164705, 2006.

[32] P. G. Etchegoin, E. C. L. Ru, and M. Meyer, "Erratum: An analytic model for the optical properties of gold," *J. Chem. Phys.*, vol. 127, no. 18, p. 189901, 2007.

[33] M. F. Pantoja, M. G. Bray, D. H. Werner, P. L. Werner, and A. R. Bretones, "A computationally efficient method for simulating metal-nanowire dipole antennas at infrared and longer visible wavelengths," *IEEE Trans. Nanotechnol.*, vol. 11, no. 2, pp. 239–246, Mar. 2012.

[34] EM Software Systems–S.A., Stellenbosch, South Africa. *FEKO Suite 7.0*, accessed on Nov. 17, 2016. [Online]. Available: http://www.feko.info

[35] Computer Simulation Technology AG, Darmstadt, Germany. *CST Studio Suite 2015*. [Online]. Available: https://www.cst.com/

[36] E. K. Miller and J. A. Landt, “Direct time-domain techniques for transient radiation and scattering from wires,” *Proc. IEEE*, vol. 68, no. 11, pp. 1396–1423, Nov. 1980.
[37] E. E. Altshuler, T. H. O’Donnell, A. D. Yaghjian, and S. R. Best, “A monopole superdirective array,” *IEEE Trans. Antennas Propag.*, vol. 53, no. 8, pp. 2653–2661, Aug. 2005.
[38] L. F. Shampine, “Vectorized adaptive quadrature in MATLAB,” *J. Comput. Appl. Math.*, vol. 211, no. 2, pp. 131–140, 2008.
[39] I. Gradshteyn and I. Ryzhik, *Table of Integrals Series and Products*. New York, NY, USA: Academic, 1965.
[40] F. W. J. Olver, D. W. Lozier, R. F. Boisvert, and C. W. Clark, *NIST Handbook of Mathematical Functions*, 1st ed. New York, NY, USA: Cambridge Univ. Press, 2010.
[41] M. Abramowitz and I. Stegun, *Handbook of Mathematical Functions: With Formulas Graphs and Mathematical Tables*. New York, NY, USA: Dover, 1964.
[42] A. P. Clarke and W. Marwood, “A compact mathematical function package,” *Austral. Comput. J.*, vol. 16, no. 3, pp. 107–114, 1984.
[43] W. F. Perger, M. Nardin, and A. Bhalla. (Jun. 1990). *Solution to the Generalized Hypergeometric Function*. [Online]. Available: http://www.ece.mtu.edu/faculty/wfp/codes/pfq.new.f
[44] D. E. Amos, “A portable package for Bessel functions of a complex argument and nonnegative order,” *Trans. Math. Softw.*, vol. 12, no. 3, pp. 265–273, 1986.
[45] S. Zhang and J. Jin, *Computation of Special Functions*, 1st ed. New York, NY, USA: Wiley, 1996.

Bingqian Lu (S’14) received the B.S. degree in electrical engineering and mathematics from The Pennsylvania State University, University Park, PA, USA, in 2014, where she is currently pursuing the M.S. degree in electrical engineering and is working on her undergraduate honors thesis.

She has been with the Computational Electromagnetics and Antennas Research Laboratory, The Pennsylvania State University, under the supervision of Prof. Werner since 2012. Her current research interests include applied electromagnetics, antenna engineering, RF and microwave engineering, and metamaterials and transformation optics.

Ms. Lu was a recipient of the Women in Math Fellowship in 2011 and the SPIE Optics and Photonics Education Scholarship in 2015.

Jogender Nagar (S’10) received the B.S. degree in electrical and computer engineering from Ohio State University, Columbus, OH, USA, in 2008, and the M.S. degree in electrical and computer engineering from Johns Hopkins University, Baltimore, MD, USA, in 2011. He is currently pursuing the Ph.D. degree with The Pennsylvania State University, University Park, PA, USA.

He was with Northrop Grumman, Linthicum Heights, MD, USA, for two years, as an Antenna Systems Engineer. He is currently a member of the Computational Electromagnetics and Antennas Research Laboratory at The Pennsylvania State University. His current research interests include computational electromagnetics, antenna theory and design, transformation optics, gradient-index lens design, multiobjective optimization, and nanoantennas.

Taiwei Yue (S’14) received the B.S. degree in physics from Nanjing University, Nanjing, China, in 2013. He is currently pursuing the Ph.D. degree in electrical engineering with The Pennsylvania State University, University Park, PA, USA.

In 2013, he joined the Computational Electromagnetics and Antennas Research Laboratory at The Pennsylvania State University, under the supervision of Prof. Werner. His current research interests include RF antenna design and measurement, RF and microwave circuit engineering, metamaterials engineering, and plasmonics.

Mario F. Pantoja (M’97–SM’12) received the B.S., M.S., and Ph.D. degrees in electrical engineering from the University of Granada, Granada, Spain, in 1996, 1998, and 2001, respectively.

He has been an Associate Professor with the University of Granada since 2004. He was a Visiting Scholar with the Dipartimento Ingenieria dell’Informazione, University of Pisa, Pisa, Italy, with the International Research Center for Telecommunications and Radar at the Delft University of Technology, Delft, The Netherlands, and with the Antenna and Electromagnetics Group at Denmark Technical University, Kongens Lyngby, Denmark. He has authored more than 50 refereed journal articles and book chapters, and more than 100 conference papers and technical reports, and has participated in more than 40 national and international projects with public and private funding. His current research interests include time-domain analysis of electromagnetic radiation and scattering problems, optimization methods applied to antenna design, terahertz technology, and nanoelectromagnetics.

Dr. Pantoja was a recipient of the 2002 International Union of Radio Science Young Scientist Award. He has received a Fulbright Grant to collaborate with the Computational Electromagnetics and Antenna Research Laboratory at The Pennsylvania State University, University Park, PA, USA.

Douglas H. Werner (F’05) received the B.S., M.S., and Ph.D. degrees in electrical engineering, and the M.A. degree in mathematics from The Pennsylvania State University (Penn State), University Park, PA, USA, in 1983, 1985, 1989, and 1986, respectively.

He holds the John L. and Genevieve H. McCain Chair Professorship with the Department of Electrical Engineering, Penn State, where he is currently the Director of the Computational Electromagnetics and Antennas Research Laboratory (CEARL: http://cearl.ee.psu.edu/) as well as a member of the Communications and Space Sciences Laboratory. He is also a Faculty Member of the Materials Research Institute, Penn State. He holds eight patents and has authored over 700 technical papers and proceedings articles, and is the author of 14 book chapters, with several additional chapters currently in preparation. He has published several books including *Frontiers in Electromagnetics* (IEEE Press, 2000), *Genetic Algorithms in Electromagnetics* (Wiley/IEEE, 2007), *Transformation Electromagnetics and Metamaterials: Fundamental Principles and Applications* (Springer, 2014), and *Electromagnetics of Body Area Networks: Antennas, Propagation, and RF Systems* (Wiley/IEEE, 2016). He has also contributed chapters for several books including *Electromagnetic Optimization by Genetic Algorithms* (Wiley Interscience, 1999), *Soft Computing in Communications* (Springer, 2004), *Antenna Engineering Handbook* (McGraw-Hill, 2007), *Frontiers in Antennas: Next Generation Design and Engineering* (McGraw-Hill, 2011), *Numerical Methods for Metamaterial Design* (New York: Springer, 2013), *Computational Electromagnetics* (Springer, 2014), *Graphene Science Handbook: Nanostructure and Atomic Arrangement* (CRC Press, 2016), and *Handbook of Antenna Technologies* (Springer, 2016). His current research interests include computational electromagnetics, antenna theory and design, phased arrays (including ultrawideband arrays), microwave devices, wireless and personal communication systems (including on-body networks), wearable and e-textile antennas, RFID tag antennas, conformal antennas, reconfigurable antennas, frequency selective surfaces, electromagnetic wave interactions with complex media, metamaterials, electromagnetic bandgap materials, zero and negative index materials, transformation optics, nanoscale electromagnetics (including nanoantennas), fractal and knot electrodynamics, and nature-inspired optimization techniques (genetic algorithms, clonal selection algorithms, particle swarm, wind driven optimization, and various other evolutionary programming schemes).

Dr. Werner is a member of the International Union of Radio Science (URSI) Commissions B and G, Eta Kappa Nu, Tau Beta Pi, and Sigma Xi. He is a Fellow of IET (formerly IEE) and ACES. He was a recipient of the 1993 Applied Computational Electromagnetics Society Best Paper Award and the 1993 URSI Young Scientist Award. In 1994, he received The Pennsylvania State University Applied Research Laboratory Outstanding Publication Award. He was a co-author (with one of his graduate students) of a paper published in the IEEE TRANSACTIONS ON ANTENNAS AND PROPAGATION, which received the 2006 R. W. P. King Award. He received the inaugural IEEE Antennas and Propagation Society Edward E. Altshuler Prize Paper Award and the Harold A. Wheeler Applications Prize Paper Award in 2011 and 2014, respectively. He also received the 2015 ACES Technical Achievement Award. He was a recipient of the College of Engineering PSES Outstanding Research Award and the Outstanding Teaching Award in 2000 and 2002, respectively. He was also awarded the IEEE Central Pennsylvania Section Millennium Medal. In 2009, he was a recipient of the PSES Premier Research Award. He was an Associate Editor of *Radio Science*, an Editor of the *IEEE Antennas and Propagation Magazine*, and an Associate Editor of the *Nature* subjournal *Scientific Reports*.